

In-orbit Vignetting Calibrations of XMM-Newton Telescopes

D. H. Lumb (dlumb@rssi.esa.int)

*Adv. Concepts & Science Payloads Office, European Space Agency,
ESTEC, 2200AG Noordwijk, Netherlands*

A. Finoguenov

*Max-Planck Institut für extraterrestrische Physik, Giessenbachstraße 1, D-85748
Garching, Germany*

R. Saxton

*XMM Survey Science Centre, Dept. of Physics & Astronomy, Leicester University,
Leicester LE1 7RH, U.K.*

B. Aschenbach

*Max-Planck Institut für extraterrestrische Physik, Giessenbachstraße 1, D-85748
Garching, Germany*

P. Gondoin

*Adv. Concepts & Science Payloads Office, European Space Agency, ESTEC,
2200AG Noordwijk, Netherlands*

M. Kirsch

*XMM Science Ops. Centre, European Space Agency, Apartado - P.O. Box 50727,
28080 Madrid, Spain*

I. M. Stewart

*XMM Survey Science Centre, Dept. of Physics & Astronomy, Leicester University,
Leicester LE1 7RH, U.K.*

Abstract. We describe measurements of the mirror vignetting in the XMM-Newton Observatory made in-orbit, using observations of SNR G21.5-09 and SNR 3C58 with the EPIC imaging cameras. The instrument features that complicate these measurements are briefly described. We show the spatial and energy dependences of measured vignetting, outlining assumptions made in deriving the eventual agreement between simulation and measurement. Alternate methods to confirm these are described, including an assessment of source elongation with off-axis angle, the surface brightness distribution of the diffuse X-ray background, and the consistency of Coma cluster emission at different position angles. A synthesis of these measurements leads to a change in the XMM calibration data base, for the optical axis of two of the three telescopes, by in excess of 1 arcminute. This has a small but measureable effect on the assumed spectral responses of the cameras for on-axis targets.

Keywords: XMM-Newton, X-ray mirrors, X-ray detectors, X-ray astronomy, CCDs

1. INTRODUCTION

XMM-Newton (Jansen et al., 2001) comprises 3 co-aligned telescopes, each with effective area at 1.5keV of $\sim 1500\text{cm}^2$, and Full Width Half



© 2018 Kluwer Academic Publishers. Printed in the Netherlands.

Maximum (FWHM) angular resolution of ~ 5 arcseconds. The 3 telescopes each have a focal plane CCD imaging spectrometer camera provided by the EPIC consortium. Two also have a reflection grating array, which splits off half the light, to provide simultaneous high resolution dispersive spectra. These two telescopes are equipped with EPIC MOS cameras (Turner et al., 2001), which are conventional CMOS CCD-based images enhanced for X-ray sensitivity. The third employs the EPIC PN camera (Strüder et al., 2001) which is based on a pn-junction multi-linear readout CCD. The EPIC cameras offer a field of view (FOV) of ~ 30 arcminute diameter, and an energy resolution of typically 100 eV (FWHM) in the range ~ 0.2 –10 keV. The two MOS telescopes are equipped with a Reflection Grating instrument (den Herder et al., 2001) that has its own dedicated readout camera.

The in-orbit calibration of the XMM-Newton mirrors has been reported elsewhere (Aschenbach et al., 2000), with special reference to the on-axis angular resolution (Point Spread Function, PSF). A second important calibration data set that is critical for analyzing spectroscopic information is the energy-dependent effective area (Aschenbach, 2002). Both these features are under constant review as a result of improving knowledge of the instrumentation, and the requirements imposed by new science investigations. In this work we concentrate on different aspects of mirror performance that must be calibrated in the context of other scientific drivers which include, for example, cluster radial brightness distribution for determining gas mass, exposure maps and counts-to-flux conversions in population studies and diffuse background normalization measurements etc.. The reduction in effective area with radial distance from the field of view centre, or vignetting, must be accurately determined to support these investigations.

To highlight the effect visually, Figures 1 and 2 show the excess flux per source detected in the 1XMM catalogue of EPIC serendipitous source detections (plotted in units of sigma). The images are displayed in the EPIC camera detector coordinates, and flux determinations assume the nominal vignetting correction centred on the reference pixel of the detector co-ordinate system (DETX, DETY in the nomenclature of the XMM data analysis system). These figures show that some low level discrepancy in the spatial variation in effective area calibration must be present.

For XMM-Newton, direct measurement on the ground of the X-ray vignetting function was prevented because nearly all X-ray beam measurements were performed in a non-parallel beam. The installation of an X-ray stray-light baffle in front of the mirrors, and the Reflection Grating Array (RGA) stack at the mirror exit plane (den Herder et al., 2001), introduced potential complications that were only measured in

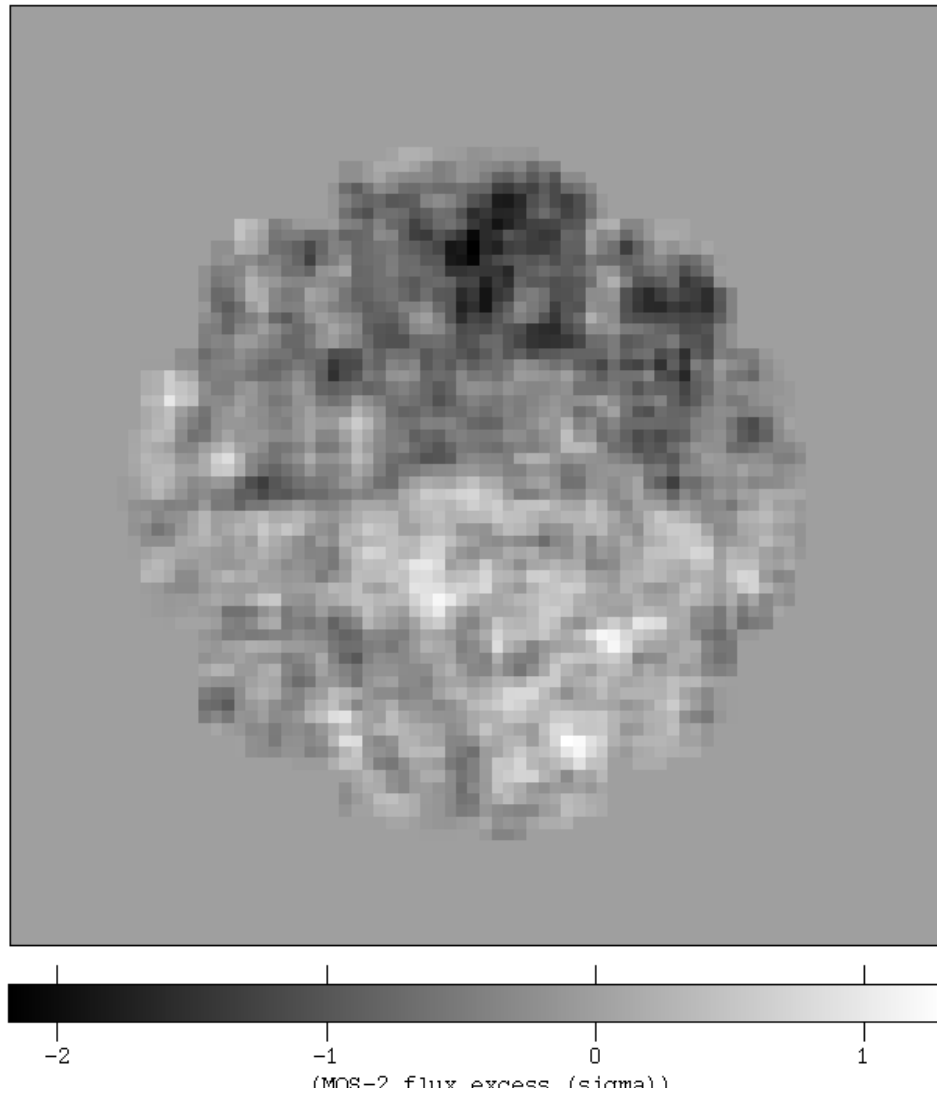


Figure 1. Image in the MOS-2 detector plane, of the mean difference in the total-band (0.2-12 keV) flux seen by MOS-2 and MOS-1 expressed in Sigma. Bright pixels indicate an excess of flux in MOS-2 and dark pixels an excess in MOS-1.

long wavelength, visible light at an EUV parallel beam facility (Tock et al., 1997).

Although the measured *geometric* vignetting factor at longer wavelengths was comparable with predictions, it was necessary to use in-orbit data to confirm the X-ray energy dependence, and check that

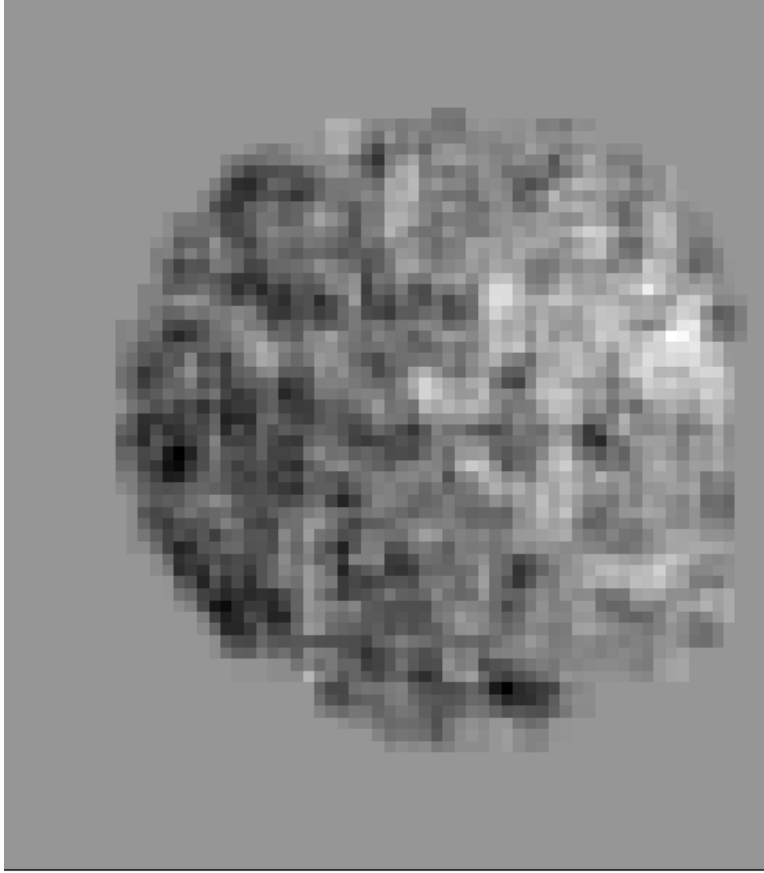


Figure 2. The equivalent image for the Epic-pn detector plane, of the mean difference in the total-band (0.2-12 keV) flux seen by Epic-pn and MOS-1 expressed in Sigma. Bright pixels indicate an excess of flux in pn and dark pixels an excess in MOS-1.

the geometric factor was maintained through the spacecraft assembly, integration, verification and launch campaigns.

2. Telescope

The design of the XMM-Newton optics was originally driven by the requirement to obtain the highest possible effective collecting area over a wide band of energies up to 10 keV. The three, nominally identical, mirror systems utilize a shallow grazing angle of $\sim 0.5^\circ$ in order to provide sufficient reflectivity at high energies. The effective area is increased by nesting 58 mirror shells in each telescope to fill the front apertures as

efficiently as possible. Both the paraboloid and the hyperboloid sections of each shell were replicated as a single piece from a single mandrel (de Chambure et al., 1996). Each telescope is complemented by an X-ray baffle, which minimizes X-ray straylight from sources outside the field of view, when rays reach the focal plane detectors by single reflection from the hyperbola.

The energy dependence of vignetting, which is superposed on any geometrical component, becomes apparent at the critical angle for grazing incidence at the off-axis angle of the target. There may be an increase in effective area again at higher energies as a consequence of the fact that only the innermost mirror shells provide substantial reflectivity. For a small diameter shell, at high energies, the area increases initially with off-axis angle: on one side of the mirror the parabola grazing angle is shallower than for the on-axis geometry. The corresponding hyperbola graze angle is then larger but because of the asymmetry of the reflectance vs. angle curve the higher reflectivity on the parabola dominates the product of the reflectances.

Each shell was individually aligned during assembly of the telescope to a design accuracy of 10's arcseconds and glued into a mounting "spider". The whole mechanical assembly was provided with alignment fiducials and optical alignment cubes and mirrors to ensure correct placement during the various activities for on-ground calibration and assembly into the spacecraft. The nominal error budget allowed for possible misalignment of the telescope axis of ~ 30 arcseconds.

Two of the three telescopes were equipped with Reflection Grating Arrays that also required alignment with the telescope axes. The three telescope assemblies were mounted on a spacecraft mirror platform that contained star trackers providing an absolute reference for the co-ordinate system of the spacecraft.

The focal plane detectors were aligned so that a reference pixel was located on the nominal telescope optical axis. In the case of the EPIC MOS cameras the reference was the central pixel of its middle CCD, while for the PN camera a dead gap at the physical centre of the camera, between CCDs, meant that the reference pixel was chosen to be slightly offset to ensure that on-axis targets were not lost onto the gap. The location of the RGA readout cameras were defined to ensure that no expected bright emission lines in dispersed spectra would fall on gaps between its CCD detectors. These reference pixels were the origin of the DETX,DETY co-ordinate system of the XMM-Newton Science Analysis System (SAS, Watson et al., 2001), in units of 0.05 arcseconds per pixel.

The physical alignment of the cameras was subject to possible error in addition to uncertainty in locating the telescope axis, and the design

had to allow also for the possibility of 10's arcsecond relative shifts due to the effects of launch loads, and eventual differential shrinkage of the carbon-fibre optical bench tube due to water vapour out-gassing in orbit. One of the first in-orbit calibration tasks was to determine the extent of any such shifts and also determine the co-alignment to the spacecraft (star-tracker) reference axis. For any observation a user could potentially request any one of six (including the Optical Monitor) instruments to be the prime, and for which a preferred detector location was defined to avoid inter-CCD gaps. The mis-alignment for each of these "boresight axes" had to be determined. Fortunately the initial mechanical alignment was sufficiently good, and preserved into orbit so that a single optimised boresight could be defined for all X-ray imaging configurations, and one for RGA spectroscopic observations. It should be highlighted that this complicated set of axis definitions is a peculiar consequence of the multiple telescope configuration of XMM-Newton compounded by the use of different instruments in the same telescopes and between different telescopes.

3. SuperNova Remnant Data

3.1. OBSERVATION CONFIGURATION FOR SNR TARGETS

The measurement of vignetting requires a compact, simple-spectrum, non-variable source at locations off-axis, with which to compare the inferred spectrum with that of the same object measured on-axis. True point sources with reasonable brightness are precluded because the effects of pile-up (Ballet, 1999) are severe, and furthermore vary with the changes in off-axis Point Spread Function (PSF), as well as with the count rate reduction due to the vignetting itself.

Extended objects require a complex ray-tracing and PSF-folding to account properly for the vignetting component. While a number of viable targets were selected for the in-orbit calibration, we have concentrated on G21.5-09 (Warwick et al., 2001) and 3C58 (Bocchino et al., 2001) for this work. The initial choice of pointing locations was complicated by the need to ensure that no significant portion of the remnants fell near CCD gaps. Given the orthogonal orientation of the two MOS cameras, together with the totally different gap patterns in the pn (Figure 3), this severely constrained the orientation available, and an angle ~ 7 degrees rotated from the nominal detector axes, and a field angle of 10 arcminutes were chosen for the initial measurements of G21.5-09.

As a consequence of the grating array angles and blocking fraction, the vignetting in the MOS cameras is expected to be a strong function

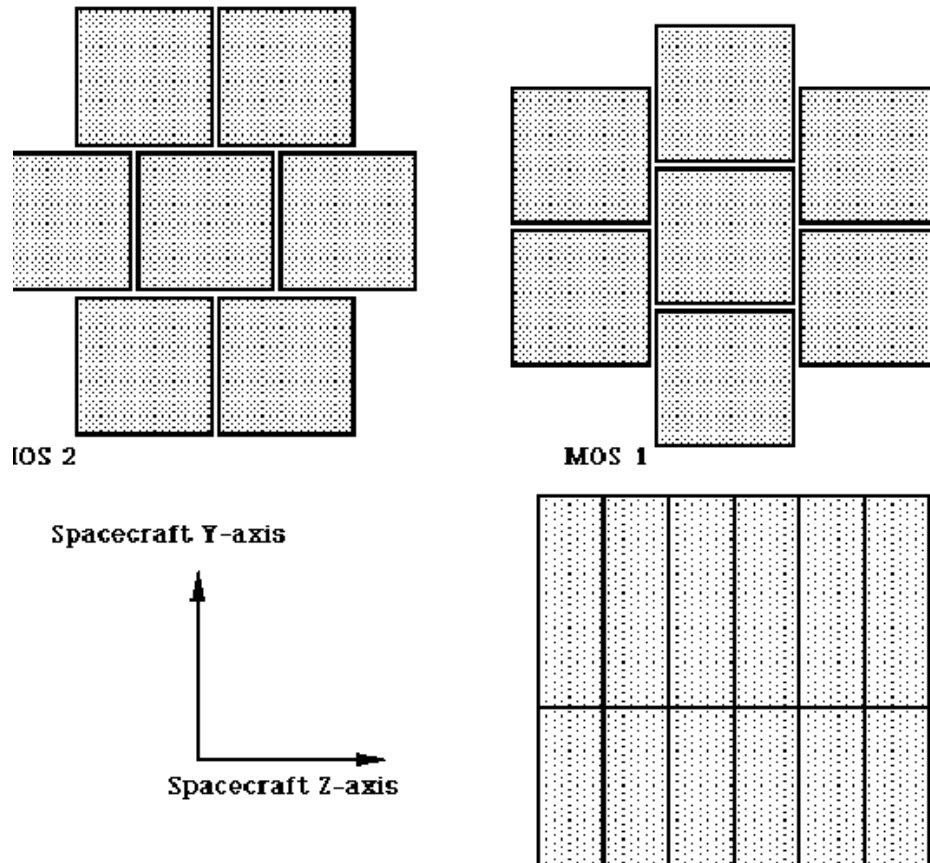


Figure 3. Schematic drawing of the CCD orientations in the 3 co-aligned EPIC cameras.

of azimuthal angle, so four locations were scheduled for G21.5-09 to sample the extreme ranges of RGA blocking (see Figure 4).

SNR G21.5-09 is a hard, bright source ideal for determining the energy dependent vignetting. A set of observations of the softer, somewhat fainter, SNR 3C58 were subsequently made to supplement the earlier observations and better sample the azimuthal dependency of the MOS camera vignetting. Measurements of 3C58 were scheduled to fall within the central CCD of the MOS cameras, to minimize the possible effect of varying quantum efficiency over the detector. Again the limitations of chip gaps cause a compromise in the actual rotations employed, such that the ensemble of pointings is as shown in Figure 5.

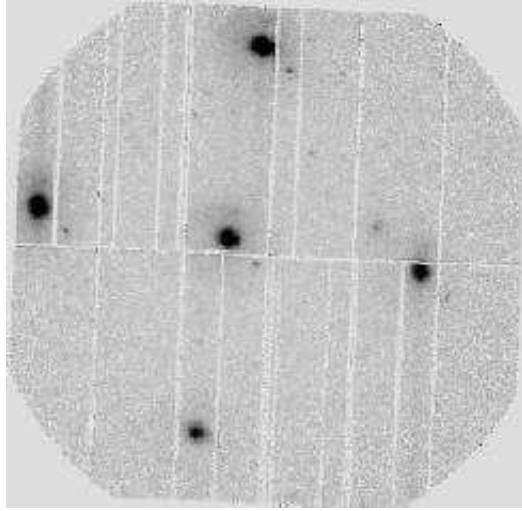


Figure 4. Merged pn image of the 5 major pointings made on G21.5-09 SNR. White gaps are physical gaps between CCDs or noisy columns

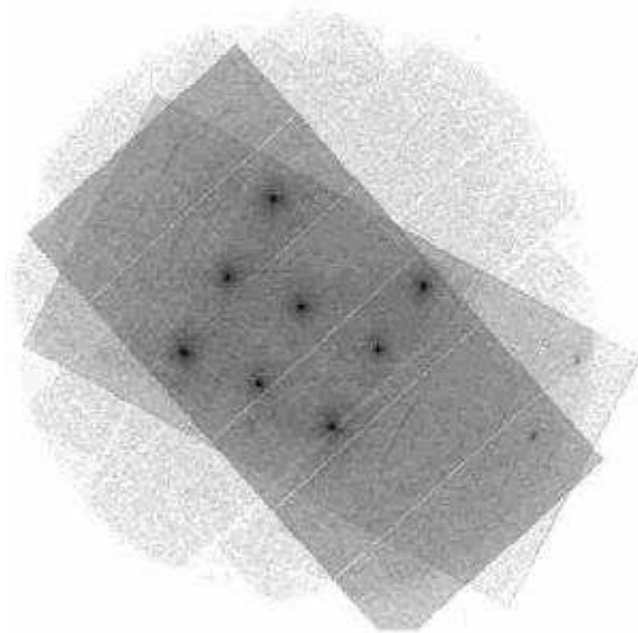


Figure 5. Merged image of the major pointings made on SNR 3C58

Table I summarises the requested pointings and observation details for these data sets

3.2. ANALYSIS OF SNR POINTINGS

Spatial regions of interest were defined around the centroid of each SNR, and fixed in sky co-ordinates for all observations, ensuring that the region was large enough compared with the PSF, but small enough to avoid a CCD gap in any single observation. Background regions of similar size were selected. Concerns about enhanced particle background in some of the observations led us to choose regions at similar field angle and azimuth to ensure representative conditions, while strict selection of low background count rate intervals minimised any systematic effects of any possible incomplete background subtraction. The analysis proceeded by determining the number of background-subtracted photon counts per energy bin at various *pseudo* on- and off-axis locations of G21.5-09 or 3C58. The relative vignetting between the corresponding locations were determined according to the count rate variations. The energy bins' widths were varied semi-logarithmically to maintain reasonable signal:noise per bin.

Table I. Summary data for the SNR observations used in the analysis

Target	Revolution	Observation ID	Date	RA 2000	DEC 2000
G21.5-09	60	0122700101	2000-04-07T12:35:28	18:33:33	-10:34:01
G21.5-09 S	61	0122700201	2000-04-09T12:22:17	18:33:40	-10:44:18
G21.5-09 W	62	0122700301	2000-04-11T12:25:38	18:32:52	-10:35:47
G21.5-09 N	64	0122700401	2000-04-15T12:25:52	18:33:26	-10:24:02
G21.5-09 E	65	0122700501	2000-04-17T12:13:09	18:34:14	-10:32:32
G21.5-09 NE	244	0122701001	2001-04-09T17:06:14	18:34:23	-10:30:40
3C58	506	0153752101	2002-09-13T04:22:11	02:05:38	+64:49:40
3C58 W	505	0153752201	2002-09-11T04:29:35	02:04:43	+64:51:13
3C58 SW	505	0153751801	2002-09-11T13:09:58	02:05:03	+64:47:38
3C58 S	505	0153752501	2002-09-11T20:03:41	02:05:23	+64:43:52
3C58 E	505	0153752401	2002-09-12T03:20:44	02:06:32	+64:48:06
3C58 NW	506	0153751701	2002-09-13T10:57:39	02:05:18	+64:53:23
3C58 NE	506	0153751901	2002-09-13T17:51:22	02:06:13	+64:51:41
3C58 N	506	0153752001	2002-09-13T23:45:05	02:05:52	+64:55:27

Unless there were gross misalignments of shells within a telescope, the vignetting in the EPIC PN telescope would be radially symmetric about its optical axis. True azimuthal variations are expected in the MOS telescopes as a consequence of differential shadowing according to the angles of the RGA grating plates. Verification of the predictions for these MOS azimuthal variations in vignetting were undermined by unexpected and significant variations ($\sim 10\%$) in relative vignetting measured in the pn camera, from azimuth to azimuth. This was attributed initially to a combination of incomplete background correction and to discrepancies in the exposure dead-time calculations influenced by the higher than nominal background. Eventually it was realised that these relative variations were correlated with camera orientations.

It was recalled that unresolved discrepancies between mirror optical alignment cube axes and inferred telescope axes measured at the EUV test facility (Stockman et al., 1997) had occurred. At the time these orientation discrepancies were claimed to be irreproducible to ~ 20 arc-second level, but were also seen in similar magnitude and direction in the Panter X-ray test facility calibration of maximum throughput orientation (Egger et al., 1997). The variation was in addition to any *fixed and systematic* offset between the mechanical and optical telescope module axes (designed to be less than 30 arcseconds). For the PN camera, we therefore simply vary the location of assumed telescope optical axis and recompute the expected vignetting function at each observed location. The axis origin is defined where the difference in low energy vignetting for all measured points is minimised.

Once reasonable agreement for the PN data was obtained, we proceeded to treat the MOS cameras in a similar manner, except in this case the azimuthal effect of RGA shadowing partially mimics a potential axis shift. We therefore *assumed* the nominal RGA performance in the calculation. In principal the two effects can not be distinguished, except:

- A gross error in RGA shadowing angles would have been detected in the dispersion relation and/or effective area of that instrument (not the case)
- For most science analysis we just need to have an empirical verification of the MOS vignetting function, whatever the cause of the azimuthal changes

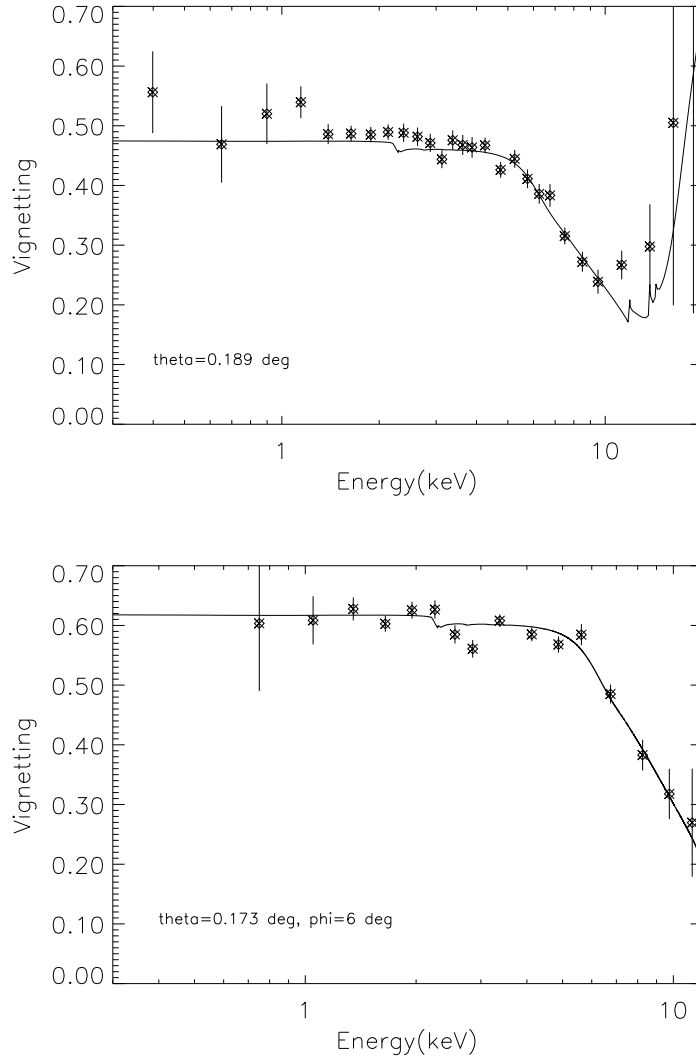


Figure 6. (a - upper) Relative (i.e. compared with nominal on-axis location) vignetting of the pn telescope for an off-axis angle of 11.3 arcminutes from the nominal boresight location. (b - lower) *Relative* vignetting of the MOS1 telescope for an off-axis angle of 10.4 arcminutes, compared with the nominal boresight location. The theoretical prediction for energy dependent vignetting is shown as a solid line in each case. This is the leftmost observation depicted in Fig 4

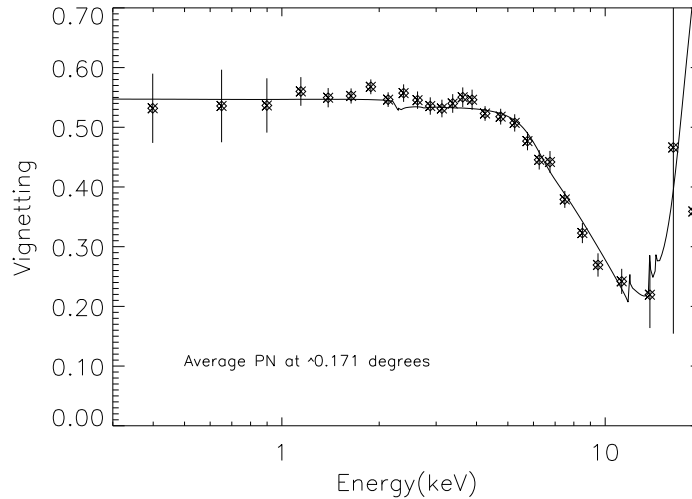


Figure 7. Relative vignetting of the pn telescope after averaging all azimuths around 10.3 arcminutes off-axis. The energy dependence is in good agreement (solid line)

3.2.1. Vignetting Results

A single azimuth vignetting measurement for the pn camera, in the lowest background exposure, is shown in Fig. 6a. A subsequent calibration observation in circa April 2001 at larger off-axis angle allowed some measure of sensitivity to the change in θ (off-axis angle), and confirms the validity of the model.

A comparable vignetting measurement for the MOS cameras is shown in Figure 6b. Due to the lower effective area of the MOS cameras, the S:N is lower than for the pn camera, and the energy scale is binned more coarsely. It was found, as with the pn camera, that there was a potential telescope axis misalignment. However records of the tests in ground facility were less clear than for those of the pn, because the installation of the RGA had blocked the access to the mirror alignment lens for most tests. Relying purely on inferred alignment of the axis based on the vignetting itself undermines the goal of directly measuring the effect of RGA azimuthal blocking factor.

3.2.2. Energy Dependence

The pn data sets were relatively close in off-axis angle and should have no intrinsic azimuthal dependence. We should be able to average the 4 separate locations of G21.5-09 to check the predicted energy dependence is correctly reproduced. This is shown in Fig. 7.

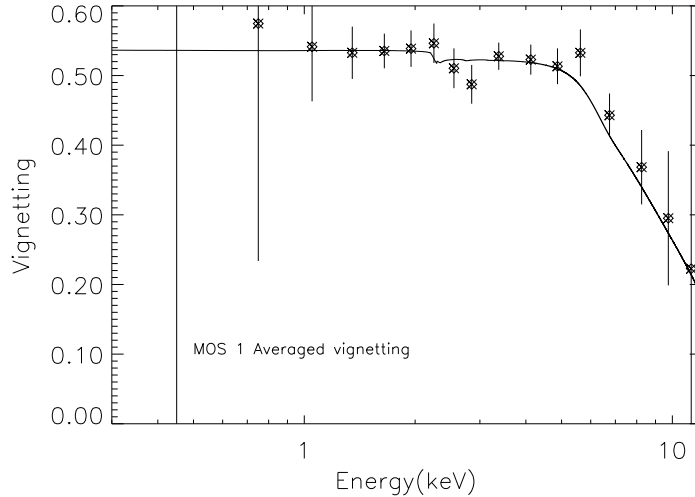


Figure 8. Relative vignetting of the MOS1 telescope after averaging all azimuths around 10.3 arcminutes off-axis. The energy dependence is in good agreement

For the MOS data, repeating the exercise is not really valid, given the large variation in RGA blocking with azimuth. However to discern if the placement of RGA gratings and ribs upsets the energy-dependent filter properties via. differential shadowing of some sub-sets of shells, we nevertheless form the same average response in the 2 MOS cases. There seem to be no significant energy-dependent discrepancies (see Figures 8 and 9).

3.2.3. Location of optical-axes

It can be seen that the energy dependence of vignetting is almost negligible in these data sets up to ~ 4 keV. Initially therefore, spectral parameters were independently found for each SNR by a joint fit of an absorbed power-law to all observations with energy range limited to $E < 4$ keV and varying normalizations per observation, in order to reduce statistical effects of spectral determination. The best-fit spectral model was then applied individually to each observation to find the relative normalizations, and the energy dependence for $E > 4$ keV. After renormalization the combined data of G21.5-09 and 3C58 were used to locate the optical axis of each camera using a minimization technique. A good fit to the predicted low energy vignetting, as a function of off-axis and azimuthal angle, was achieved by applying a small shift in the optical axis position for MOS-1 (Fig. 10). A larger offset, of the order

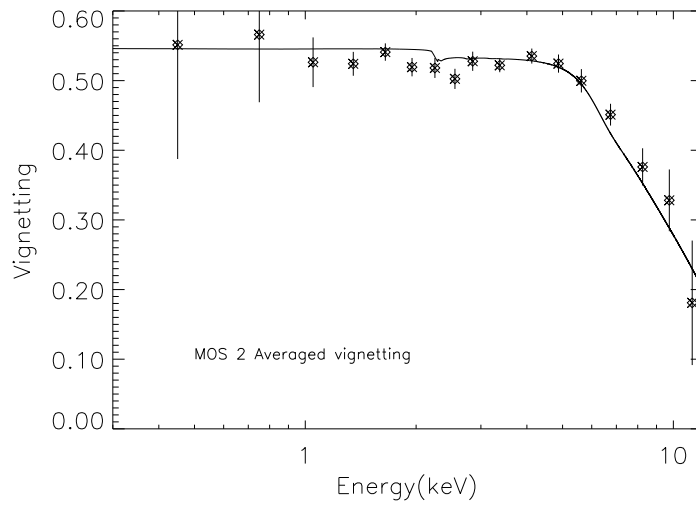


Figure 9. Relative vignetting of the MOS2 telescope after averaging all azimuths around 10.3 arcminutes off-axis. The energy dependence is in good agreement

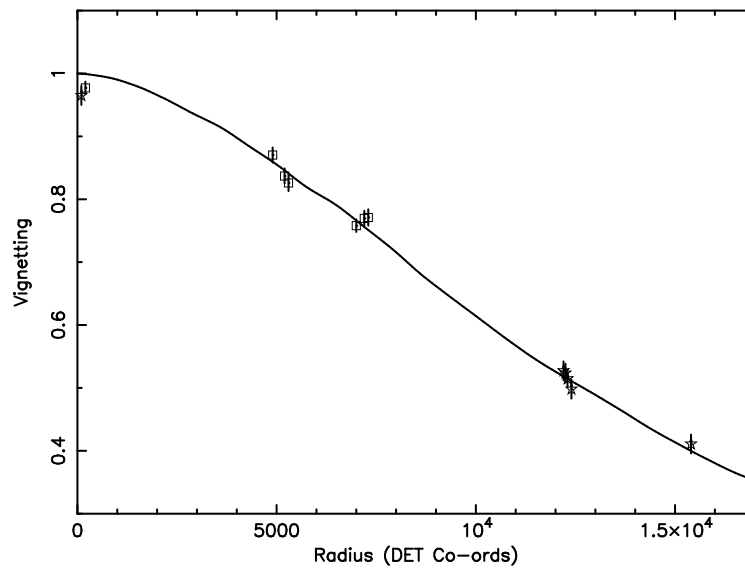


Figure 10. Comparison of G21.5-09 (stars) and 3C58 (squares) MOS-1 data with the expected mirror vignetting, centered at DETX=200, DETY=-50. The data have been corrected for RGA blocking.

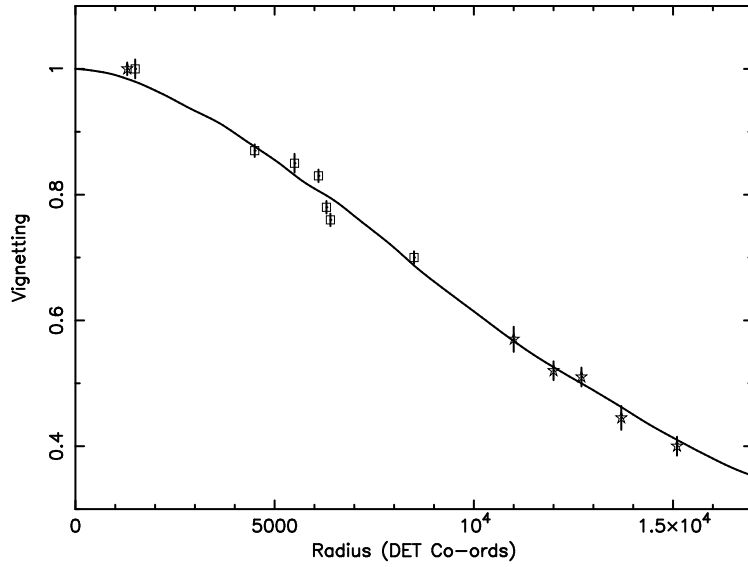


Figure 11. Comparison of G21.5-09 (stars) and 3C58 (squares) MOS-2 data with the expected mirror vignetting, centered at DETX=340, DETY=-1300. The data have been corrected for RGA blocking.

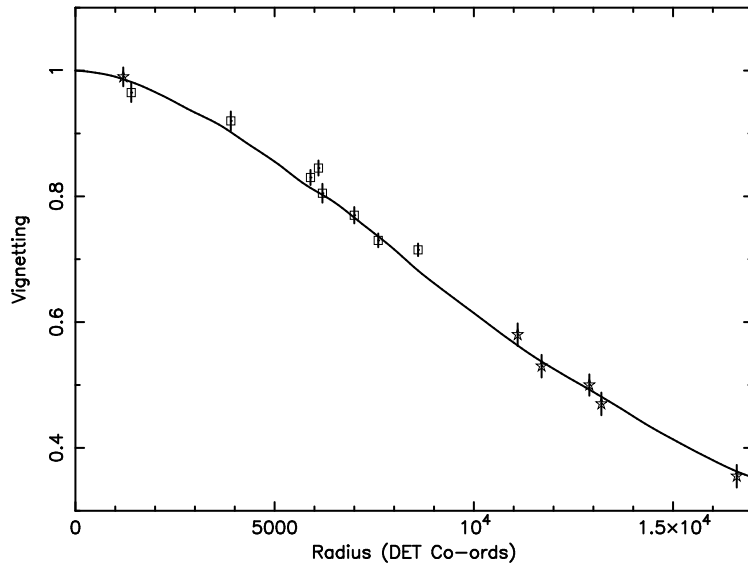


Figure 12. Comparison of G21.5-09 (stars) and 3C58 (squares) pn data with the expected mirror vignetting, centered at DETX=1300, DETY=450.

of 1 arcminute, was found to be necessary to obtain a good fit for the MOS-2 and pn telescopes (Figs. 11,12).

4. Alternative Measurements

In order to provide corroborating evidence for these axis shifts, different measures were proposed.

4.1. SOURCE ELONGATION

The PSF broadens with off-axis angle, especially in a direction perpendicular to a vector connecting the source and optical axis positions. A plot of source PSF elongation versus off-axis angle should therefore be symmetrical about the optical axis. We selected a large sample of serendipitously detected sources, after removal of non-point-like objects, from the 1XMM catalogue, for each camera. Figure 13 shows the variation of this elongation with off-axis angle for the pn sample. The centroid of the distribution was found by minimizing the function:

$$E = A + B\theta^2 + C\theta^4$$

where E is the measured elongation, θ the off-axis angle measured from the telescope axis and A, B and C are coefficients.

The elongation E was defined as follows:

- the source image out to a cutoff radius of 20 arcsec was resampled in source-centric polar coordinates r and ϕ ;
- the resulting image was multiplied by r to preserve scaling, then Fourier-transformed in the ϕ coordinate;
- the ratio between the magnitudes of the 0^{th} and 2^{nd} Fourier coefficients was taken as the elongation.

The best fit centroids reveal a qualitatively similar axis shift to that measured with G21.5-09 and 3C58. The measured values are: PN (DETX,DETY = 1140,340), MOS1 (DETX,DETY = -320,+540) and MOS2 (DETX,DETY = -340,-1700).

A small discrepancy was noted for the MOS cameras, again suspected to be due to the effects of the RGA assembly. A raytrace for a nominal XMM telescope was made, in which multiple sources were traced through to the focal plane, and then their elongations in focal spot determined as a function of position in the focus, by simple Gaussian fitting. For an unobscured telescope, the minimum elongation

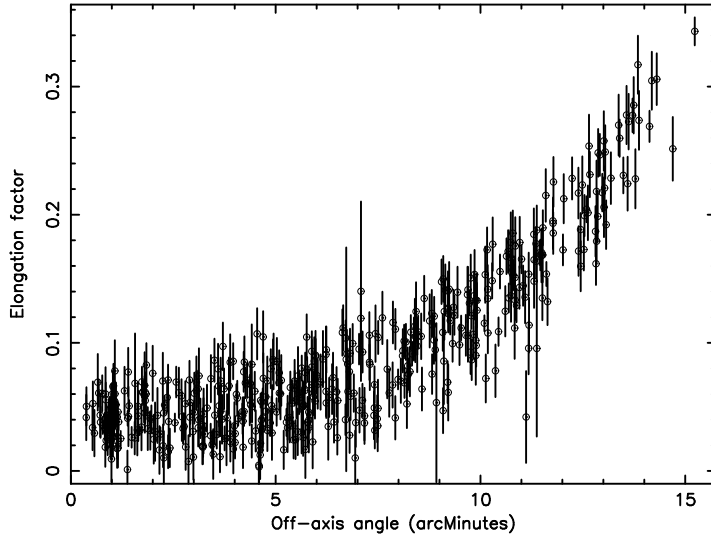


Figure 13. Relative elongation of point sources in the pn camera as a function of off-axis angle

occurred at the centre of the focal plane. However for a telescope fitted with a nominal RGA structure, the minimum elongation occurred off-axis, in a direction parallel with the dispersion axis. It is believed this can be attributed to shadowing of rays that are intercepted by the grating plates, restricting the scattering (and hence elongation) in a direction parallel with the dispersion direction. As the RGA plates are angled to the telescope axis, the location of elongation minimum is hence offset. The ray trace estimate of this offset is about 22 ± 1 arcsec.

4.2. DIFFUSE BACKGROUND

In (Lumb et al., 2002), the compilation of a set of data from high galactic fields was described. After exclusion of individual point sources, this field represents the average properties of the diffuse Cosmic X-Ray Background (CXB). Although this background represents the superposition of many unresolved faint sources, the averaging over several fields with XMM-Newton ensures any “cosmic variance” is minimized, and the artificial field should be very uniform. In such a case the centroid of surface brightness distribution should map to the optical axis of maximum throughput.

This is difficult to interpret in the case of the MOS cameras in particular because the apparent vignetting varies in a direction parallel to the grating array dispersion direction. The differential blocking of

the grating must therefore be unfolded from any potential telescope axis tilt effects.

The data set from high galactic latitudes was binned into images in the energy band 0.5–4keV for each camera. The surface brightness distribution was projected in detector X, and Y co-ordinates and was corrected for exposure effects (bad pixels, CCD gaps, CCD dead times etc.). Next the predicted amount of RGA blocking as a function of θ, ϕ was calculated by raytrace, and divided into the surface brightness profiles. The centroid of brightness was then calculated by a polynomial fit. See as an example Fig. 14.

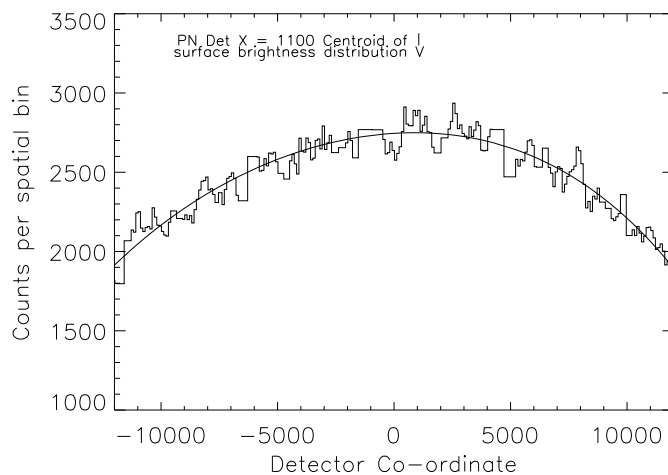


Figure 14. Surface brightness (0.5–4 keV) in spatial bins of the merged image of several high latitude background fields. The solid curve is the best polynomial fit. The lack of symmetry is attributed to the offset of the circular aperture of the camera from the centre of the telescope

The main weakness of this approach is that the RGA blocking is assumed to be correctly modeled, and not left as a free parameter. The justification is supported by the nominal performance of the RGA dispersion properties as measured in-orbit by the spectrometer instrument.

4.3. COMA CLUSTER

The Coma cluster of galaxies is one of the brightest diffuse X-ray objects on the sky, filling the field of view of XMM-Newton detectors. An additional possibility to calibrate the vignetting of the mirror system of

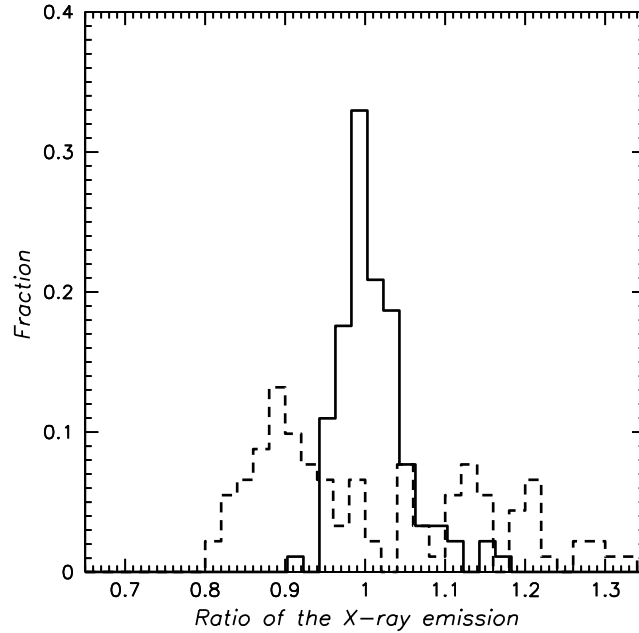


Figure 15. Ratio of surface brightness (0.5–2 keV) in spatial bins of the Coma Cluster, for two different camera orientations. *Dotted line* - vignetting corrected with initial calibration. *Solid line* - vignetting corrected according to improved estimate of telescope axis

Epic pn is provided by performance of a special calibration observation of the Coma centre in addition to the existing set, described in Briel et al. (2001). The idea is to use the same region on the sky but with a position angle of ~ 120 degrees between observations. In this case a vignetting miscalibration producing an under-corrected part of the emission in the first observation will be compared to over-corrected part in the second. In case of the shift of telescope axis, such deviations occur symmetrically, so that a ratio map of the two images has one side of the image being larger and the other smaller than unity.

Additional fluctuations on the ratio map are introduced unless OOTE (Out-Of-Time Events) subtraction is performed. This is a specific feature of the pn camera (compared to MOS where OOTE are small in fraction), where events are accumulated in the CCD while the previous image frame is still being read out. The OOTE may be removed statistically, using off-line products generated by XMMSAS *epchain* program for every observation. In this particular instance the importance of OOTE is caused by a change in the read-out mode for pn in

the second observation to full frame from extended full frame mode, that was employed for the other XMM Coma observations, such that this fraction of smeared events changed from 0.023 to 0.063.

We choose the 0.5 – 2 keV band for the primary analysis, while energy-dependent effects were checked using the 0.25 – 0.5 keV and 5 – 7.9 keV bands, considering previous data from mirror test results from the PANTER facility as well as the presence of strong background lines > 7.9 keV.

In order to achieve good statistics a binning of 32×32 of original pn pixels was employed (128×128 for MOS). Border pixels in this binning can have much lower fraction of valid pixels and were excluded from the analysis. The best telescope position was chosen to achieve the lowest scatter among about a hundred independent points of the image ratio map, for both pn and each MOS camera. The effect of the change in the position of the telescope axis was emulated in the calibration version of the exposure map, where by changing the vignetting we still retain proper position of the detector chips.

In detail the procedure comprised two main parts: preparation of the dataset and a loop of calculations repeated with varied input position of the telescope axis to minimize the spread in the dataset points.

The data preparation part comprised:

- screening both observations for background flares, as described in Briel et al. (2001).
- for both observations extracting source and OOTE images in the 0.5 – 2 keV band
- Correcting both images for OOTE
- subtracting the instrumental background, using Filter Wheel Closed background accumulation (for description of this background dataset see e.g. (Lumb et al., 2002))
- Translate the image for one observation to the reference frame of the other
- Calculate the mask file where both observations have sufficient data. Only $FLAG = 0$ events are considered (large detector gaps). Also only the pn event types with $PATTERN < 5$ are considered.
- Discard image pixels absent in at least one observation, using the cross-correlation of the mask files for both observations. The resulting mask file is retained to be later applied to experimental exposure maps.

- bin the image to achieve good statistics.

The calibration loop comprised:

- For input parameters of the test telescope axis position create exposure maps for both observations
- Normalize the exposure map to correct for loss of the flux due to subtraction of OOTE, by multiplying the maps by $(1 - f_{OOTE})$, 0.937 and 0.977 for full and extended full frames, respectively
- Translate the exposure map for one observation to the reference frame of the other
- Discard exposure pixels absent in at least one observation, using the pre-calculated mask file
- Bin the exposure maps in accordance to binning of the image
- De-vignette the images and produce their ratio
- estimate the dispersion around the mean. The position of the telescope axis is searched to minimize this dispersion.

Uncertainty in the parameter estimate is calculated using 90% confidence level estimate for the χ^2 method. However the systematic uncertainty seems to drive the error, and is related to an astrometric uncertainty for the position of each image.

Epic pn data comparison shows a very small dispersion at a telescope axis position ($DETX = 1243 \pm 30$ pixels $DETY = 402 \pm 30$) pixels in detector coordinates. The one-dimensional scatter of pixels around the mean is plotted in Figure 15. Note that the mean value of 1.000 is not enforced and is an additional argument in favor of the method. The original calibration introduced a 14% r.m.s. scatter in the surface brightness data, while the proposed revised calibration decreases the r.m.s. to 3%, comparable with the statistical noise. This result is consistent with the large r.m.s. scatter found in pn-MOS1 comparison of serendipitous sources (see Figures 1 and 2 and Saxton, 2002).

Table II illustrates the quality of the calibration.

A change in the position twice the quoted error bar, presented in Table II above produces noticeable changes on the image being dimming and brightening of the opposite sides. Variation in the background level can introduce additional 1% errors for furthest from on-axis pixels.

The adopted error on the position of the telescope axis includes various systematics e.g. caused by the small misalignment between the two Coma pointings and changes in the instrumental background

Table II. Residual dispersion in the pn vignetting calibration.

Radius arcmin	Dispersion, %	
	best fit	at 2 sigma deviation
8–11	3.712	3.826
4–8	2.376	2.422
0–4	2.186	2.199

level, while the formal statistical error is smaller, 10 pixels. However, the precision at which the position of the telescope axis is achieved exceeds by far the typical resolution at which e.g. the exposure maps are calculated (200 DETX/DETY pixels or 10 arcseconds).

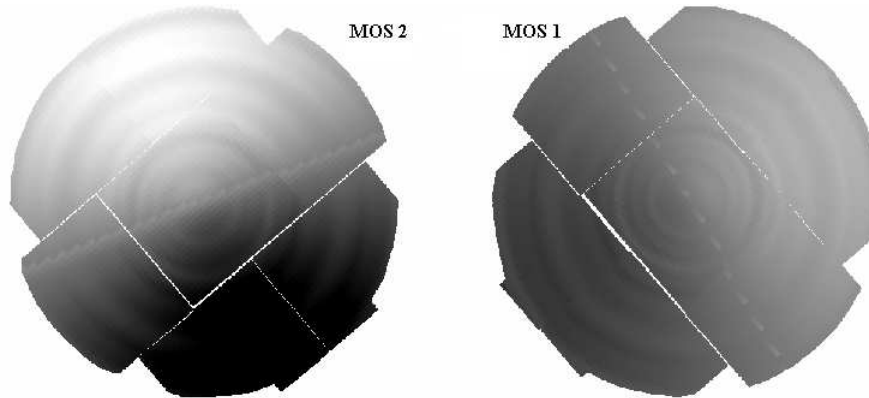


Figure 16. Ratio of the new and old exposure maps for MOS 1 and 2, showing the amplitude and direction of the change. Fine structure on these images (a line and annuli) is an artifact produced by finite precision at which the exposure maps are generated. Vignetting is azimuthally symmetric, while the line-like feature of CCD gaps are parallel to the direction of equal RGA transmission, and not this vignetting shift.

4.4. CALIBRATING MOS VIGNETTING USING THE COMA OBSERVATIONS

Calibration of the MOS vignetting using the Coma cluster has been first done by cross-calibration with pn and later repeated using a self-calibration method, as has been described above for pn. Table III lists three independent measurements of the positions of the telescope axis obtained using both Coma MOS observations, 2001 and 2000 denoting the MOS-pn comparison, using the year of MOS observation to describe

the observational dataset, the 'average' of the two and 2000 vs 2001 'self' calibration of MOS.

Table III. Positions of the MOS telescope axis from the analysis of Coma cluster. Units are internal camera values of 0.05 arcsecond.

Dataset	DETX	DETY	Dispersion, %
MOS2			
2001	653 ± 60	-1260 ± 30	4.50
2000	440 ± 60	-1250 ± 30	4.65
average	550 ± 60	-1255 ± 30	
self	492 ± 60	-1256 ± 30	4.73
MOS1			
2001	136 ± 40	-134 ± 70	4.56
2000	87 ± 40	-281 ± 70	4.76
average	110 ± 40	-200 ± 70	
self	159 ± 40	-303 ± 70	4.68

The difference in the normalization between 2000 and 2001 MOS1 observations amounts to 6%, and is due to differences in the best-fit positions. The self-calibration finds the mean flux ratio between two observations of 1.005, which is acceptable. The similarity of the results of cross and self calibration of MOS is reassuring and demonstrates negligible effect of possible chip-to-chip sensitivity variations for MOS. However, the dispersion achieved in the best-fit position is worse, compared to pn results and could partly be caused by lack of fidelity in the description of the RGA shadowing in the current version of SAS.

Fig.16 shows the magnitude of the proposed changes in the vignetting for MOS 1 and 2 cameras. Only a small change is proposed for MOS 1, while vignetting for MOS 2 is substantially revised. The effect of RGA-vignetting degeneracy reduces the sensitivity of the method to the absolute value of the telescope shift, yet the direction of the shift is rather well determined. Since the problem originates in the low contrast in the exposure map, caused by these changes, it implies little importance of the precision in the MOS calibration to absolute flux measurements, however, a possible caveat could be larger uncertainty in the energy-dependent vignetting effects, that are important at energies > 5 keV. Achievement of the agreement in the MOS position with other calibration methods presented in this paper is therefore of importance.

Table IV. Summary of the different axis displacement values for the EPIC cameras inferred with the various measurement techniques. Units are internal camera values of 0.05 arcsecond in “Detector” coordinates.

Instrument coordinate	M e t h o d			
	G21.5-09/3C58	Source Elongation	Diffuse Background	Coma
pn DET X	1300 ± 300	1140 ± 200	1100 ± 300	1243 ± 30
pn DET Y	450 ± 300	340 ± 200	400 ± 300	402 ± 30
MOS-1 DET X	200 ± 300	-320 ± 200	0 ± 200	110 ± 40
MOS-1 DET Y	-50 ± 300	540 ± 200	0 ± 200	-200 ± 70
MOS-2 DET X	340 ± 300	-340 ± 200	300 ± 200	550 ± 60
MOS-2 DET Y	-1300 ± 300	-1700 ± 200	-1300 ± 200	-1255 ± 30

4.5. COMPARISON OF METHODS

The main method is important in that it defines rather well the energy dependent effect of the vignetting but gave some concerns about the rather large offset in telescope axis. The later methods give confidence that this offset is real, and give similar magnitudes for the effect.

Table IV summarises the inferred axis shifts from these different existing measurements.

The discrepancy in axis value obtained by source elongation method for the MOS cameras is partly explained by the differential shadowing of RGA stack that modulates the PSF shape. this was modelled by ray trace as described in section 4.1. The RGA dispersion direction is parallel with the MOS1 detector -Y axis, and the MOS2 detector +X axis. The calculated shift due to differential shadowing amounts to $\sim 440 \pm 20$ units, which reduces the discrepancy in that axis to $\sim 1\sigma$. The discrepancy in the orthogonal direction is not explicable by the ray trace, but is only $\sim 2\sigma$. Additional systematic uncertainty may be brought about by the non-circular shape of the PSF (roughly pentangle and triangle shapes for MOS1 and MOS2 respectively) that is invariant with field angle and due to some distortion encountered on mounting the mirrors to the spacecraft interface plate.

5. CONCLUSIONS

The energy dependent vignetting calibration can be well matched to pre-launch predictions, but only on an assumption that the telescope

optical axis is not perfectly aligned with the telescope boresight. This is not unexpected following difficulties on-ground of maintaining and/or measuring the telescope axis to better than 10's arcseconds. We note that the assumed telescope axis misalignment implies that "on-axis" targets at the common boresight location are actually at a slightly different vignetting value per telescope. We speculate that this partly accounts for some of the observed flux discrepancies between the MOS and pn cameras (Figure 17). After reviewing these data sets, it was decided that the XMM-Newton calibration database would be updated in 2004 to account for new reference axes to be centred at PN (DETX,DETY = 1240,400), MOS1 (DETX,DETY = 100,-200) and MOS2 (DETX,DETY = 500,-1250).

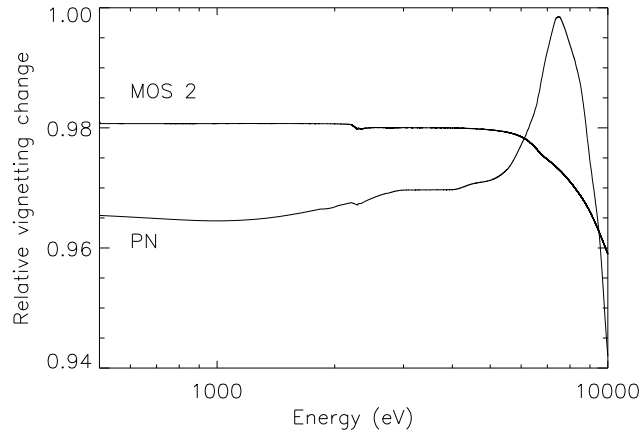


Figure 17. Ratio of uncorrected and vignettted effective areas for an on-axis target. The flux differences for typical 0.5-2keV band will be \sim a few % for typical objects, and a small difference in recovered spectral slope will be caused by the change with energy

6. Acknowledgments

All the EPIC instrument calibration team who have contributed to understanding the instrument are warmly thanked for their efforts. We thank the XMM-Newton Science Operations Centre team for their help in scheduling the calibration observations that needed special arrangements. AF acknowledges receiving the Max-Planck-Gesellschaft Fellowship. *XMM-Newton* is an ESA science mission with instruments

and contributions directly funded by ESA Member States and the USA (NASA).

References

- Aschenbach, B., Briel, U., Haberl, F., et al. 2000, Proc. SPIE, 4012, 731
 Aschenbach, B. 2002, Proc. SPIE, 4496, 8
 Ballet, J. 1999, A&A Suppl, 135, 371
 Briel, U.G., Henry, J.P., Lumb, D.H. et al. 2001, A&A 365, L60
 Bocchino, F., Warwick, R. S., Marty, P., et al. 2001, A&A, 369, 1078
 de Chambure, D., Laine, R., van Katwijk, K., et al. 1996, Proc SPIE 2808, 362
 den Herder, J. W., Brinkman, A. C., Kahn, S. M., et al. 2001, A&A 365, L7
 Egger, R., Aschenbach, B., Bräuninger, H. et al. 1997, Panter Test Reports XMM-TS-PA063/970829, XMM-TS-PA070/980115 etc.
 Jansen, F., Lumb, D.H., Altieri, B. et al. 2001, A&A 365, L1
 Lumb, D.H., Warwick, R.S., Page, M., and de Luca, A., 2002, A&A, 389, 93
 Saxton, R.D. 2002, XMM-Science Ops Centre Technical Note XMM-SOC-CAL-TN-0023
 Stockman, Y., Tock, J-P., Thome, M., et al. 1997, CSL Test Reports, RP-CSL-MEV-97032, RP-CSL-MEV-97019 etc.
 Strüder, L., Briel, U., Dennerl, K., et al. 2001, A&A, 365, L18
 Tock, J-P., Collette, J-P. and Stockman, Y., Proc. SPIE 3114, 554
 Turner, M.J.L.T., Abbey, A., Arnaud, M., et al. 2001, A&A, 365, L27
 Warwick, R.S., Bernard, J.-P., Bocchino, F., et al. 2001, A&A, 365 L248
 Watson, M.G., Augueres, J-L., Ballet, J. et al., 2001, A&A 365 L51

